A model for the Artic mixed layer circulation under a summertime lead: Implications on the near-surface temperature maximum formation

Alberto Alvarez

5   NATO-STO Center for Maritime Research and Experimentation-CMRE, V. San Bartolomeo 400, La Spezia, 19126, Italy

Correspondence to: Alberto Alvarez (alberto.alvarez@cmre.nato.int)

Abstract. Leads in the sea ice sheet have been studied extensively because of their climate relevance. In summer, there is an intense heat exchange between the ocean and the atmosphere in the leads. Leads are also preferential melting sites in early summer, but their oceanography and climate relevance, if any, remains largely unexplored during this period of the year. In

10   particular, the development of a near-surface temperature maximum (NSTM) layer at typically 10-30 m deep under different Arctic Basins, has been related observationally to the penetration of solar radiation through the leads. The observations reveal that the concatenation of calm and wind events in the leads could facilitate the development of the NSTM layer. This study investigates, using numerical modelling and an idealized framework, the formation of the NSTM layer under a summer lead exposed to a combination of calm and moderate wind periods. During the calm period, solar heat accumulates in the upper

15   layers under the lead. Near-surface convection cells are generated daily, extending from the lead sides to its center. Convection cells affect the heat storage in the mixed layer under the lead and the adjacent ice cap. A subsequent wind event (and corresponding ice drift) mixes and spreads fresh and cold meltwater into the warm layers near the surface. Surface mixing results in temperatures in the near-surface layers that are lower than in the deeper layers, where the impact of the surface stresses is weaker. Also, the warm waters initially located under the lead surface stretch and spread horizontally. Thus an

20   NSTM layer is formed. The study analyses the sensitivity of depth and temperature of the NSTM layer to buoyancy forcing, wind intensity and ice drift. Numerical results suggest that the NSTM layer appears with moderate wind and ice drift, and disappears when wind intensity is higher than 9 ms^{-1}. According to the results, ice drift is key in the development of the NSTM layer.

25   **Copyright statement:** The author's copyright for this publication is transferred to the NATO STO Centre for Maritime Research and Experimentation (NATO STO CMRE).

1 Introduction

The Arctic Ocean is currently responding to changes in atmospheric and oceanic processes associated to climate change, by a rapid retreating of sea ice (Liu et al., 2013; Stroeve et al., 2007). Ice retreating not only affects the local Arctic environment,

30   but also has a feedback on the global climate. Ice melting might influence climate components like the increase of abnormal weather events in the Northern Hemisphere and the modifications in the stability of the thermohaline circulation, among others (Levermann et al., 2007; Vihma, 2014).

Sea ice loss involves heat transfers in the ice-atmosphere-ocean system mediated by physical mechanisms such us the atmospheric and oceanic heat transports (Zhang et al., 2008; Spielhagen et al., 2011), variations in water vapor and cloudiness

35   (Schweiger et al., 2008), or modifications in the sea ice cover (Screen and Simmonds, 2010). In particular, cracks in the sea ice sheet (also known as leads) are ice-free areas where strong heat and chemical exchanges occur between the ocean and the atmosphere (Maykut, 1978; Alam and Curry, 1995; Douglas et al., 2005; Kort et al., 2012; Steiner et al., 2013). Leads are typically generated by stress-deformation events in the continuous sea ice sheet. These events develop elongated, recurring

structures of open water and thin ice. Their geometry ranges from 10 m to 1 km wide and up to 100 km long (Wilchinsky et

40   al. 2015). Due to their climate relevance, a number of studies have considered the identification and characterization (width, orientation, area of coverage and spatial distribution) of leads in the ice sheet (Barry et al., 1989; Miles and Barry, 1998; Brohan and Kaleschke, 2014; Wernecke and Kaleschke, 2015; Hoffman et al. 2019).

In winter, leads rapidly refreeze with frazil ice production due to large heat fluxes from a relatively warm ocean exposed to cold air. The refreezing of the lead produces a buoyancy flux by brine rejection, which generates a particular circulation pattern

45   at the lead location: the dense water flows away from the lead when it reaches the bottom of the mixed layer while freshwater flows in from the lead sides near the surface (Kozo, 1983; Morison et al, 1992; Morison and McPhee, 1998). Salt rejected by brine rejection constitutes a major salt input to the Arctic mixed layer (Morison and Smith, 1981; Lemke and Manley, 1984; Morison et al, 1992).

In the early melting season, leads become preferential melting sites (Perovich et al., 2001). This is because the new ice in the

50   leads is thinner and has a lower albedo than the adjacent ice (Grenfell and Maykut, 1977; Tschudi et al., 2002). Additionally, lead locations are topographically lower, accumulating meltwater and further reducing albedo. Perovich et al. (2001) found that ice in the leads melts almost completely by the end of July. At this time, the ice landscape is made up of large plates separated by long, narrow open leads. As the thermal deterioration of the sea ice progresses, this landscape transforms into a complex mosaic of floes intertwined with open waters (Perovich et al., 2001).

55   The development of a near-surface temperature maximum (NSTM) layer at typically 10-30 m deep under different Arctic Basins, has been attributed to the penetration of summer solar radiation through leads (Maykut and McPhee, 1995; Jackson et al., 2010; Kadko, 2000). The temperature in the layer is usually more than one or two tenths of a degree above the underlying temperature or the freezing point, respectively (Jackson et al., 2010; Steele et al., 2011). An NSTM layer would result from solar heating beneath a protective halocline generated by fresh water accumulated by melting sea ice. Strong near-surface

60   stratification would preserve the NSTM layer for long periods, likely affecting the oceanographic structure and acoustic properties of the upper ocean and overlying ice cover. For example, the NSTM layer could significantly enhance sea ice melt from turbulent heat fluxes to the basal ice caused by wind or ice motion (Ramudu et al., 2018). Sound ducts with a significant capacity for long-range acoustic propagation may also result from the formation of the NSTM layer (Freitag et al., 2012).

Some observational evidence correlates the development of the NSTM layer with a combination of buoyancy and wind events

65   in the leads (Gallaher et al., 2017). Under quiescent conditions, a warm layer of fresh water on the surface of the summer leads is the result of the combined effect of meltwater runoff and solar heating (Richter-Menge et al., 2001; Gallaher et al., 2017). This warm freshwater layer deepens and spreads laterally under adjacent ice if calm conditions persist (Richter-Menge et al., 2001). Wind events after the calm period induce further mixing of the warm freshwater layer with the underlying ocean, when wind and/or ice speeds reach a threshold (Richter-Menge et al., 2001). Wind and/or ice drift erode and deepen the warm

70   freshwater layer in the summer lead. However, the summer halocline would protect the warm layers from the action of wind and ice (Gallaher et al., 2017). Therefore, the sequence of calm periods and moderate winds can develop an NSTM layer under the summer leads.

Numerical studies on leads in summer are scarce in the literature. Skyllingstad et al., (2005) provided insight on lateral melting processes in a summer lead using a large-eddy simulation (LES) model. The numerical study suggests that lateral melt rates

75   increase with lead size, but decrease in high winds due to turbulent mixing with cold waters residing beneath the sea surface. Ramudu et al., (2018) also used a LES model to investigate numerically the relevance of heat turbulent fluxes from the mixed layer on sea ice melt in a summer lead. The results evidenced the heat entrainment from a warm layer near the surface that generally forms in summer at different Arctic locations. The author is not aware of other numerical studies in summer leads. In particular, the development of an NSTM layer in a summer lead under a sequence of calm and wind conditions still remains

80   numerically unexplored.

This study investigates the dynamics in a summer lead exposed to a sequence of calm and moderate wind conditions such as those reported in Richter-Menge et al. (2001) at ice station SHEBA from July 18th to July 31st 1998. An axisymmetric geometry and a particular thermodynamic forcing are common features to summer leads in calm conditions. For this reason, the study initially focuses on the circulation under a summer lead resulting from the combined effect of lead geometry, solar

85 radiation and sea ice melt. Under these conditions, lateral buoyancy gradients between the edges and center of the lead due to solar heating and ice melt can trigger a circulation in the lead. This circulation would result in a warm layer of fresh water on the surface of the lead. The study is then completed with the analysis of the mixing and deepening, if any, of the warm freshwater layer due to wind events (and associated sea ice drift) after the calm period. The ultimate goal of the study is to assess if these environmental conditions could result in the formation of the NSTM layer as inferred from the observations.

90

2 Methodology

2.1 The physical model

The conceptual framework considers a vertical cross-section of an ice landscape described by recurring and large sea ice plates separated by long, narrow, rectilinear leads. The ice landscape is idealized by a fringe pattern with ice-patches and open water

95 leads of 250 m and 50 m wide, respectively, Figure 1. Field observations reveal that the maximum occurrence of lead geometry corresponds to leads and refrozen leads less than 100 m wide (Barry et al., 1989, Tschudi et al., 2002) and distances between leads less than 500 m (Haggerty et al., 2003). Therefore, the selected geometry attempts to be representative of the main lead fraction.
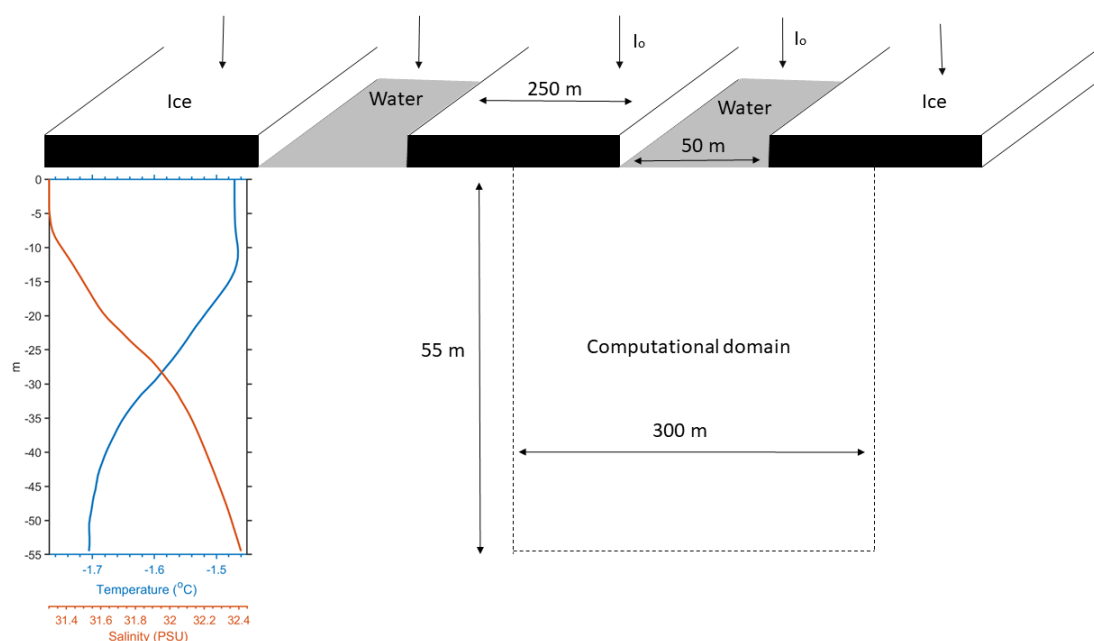
100

Figure 1: Idealized framework of the current study, showing the incoming solar radiation, I_o, and initial profiles of temperature and salinity, respectively.
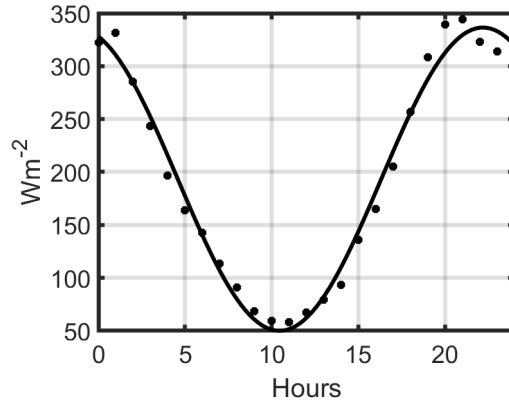
105

Figure 2: Daily incoming shortwave radiation obtained by averaging records from July 18th to 26th, 1998 at SHEBA Ice Station (Persson et al., 2002). Averaged data is represented by the black dots. Solid black line fits the raw data to a periodic function with a least-squares method.

110

The ice plates are assumed to be stationary in the calm period and drift during the subsequent wind event. Reference temperature (T_{ref}) and salinity (S_{ref}) profiles were obtained by averaging daily conductivity, temperature and depth measurements (CTDs) collected at the ice station SHEBA from July 18th to July 26th 1998 (Stanton and Shaw, 2006), Figure 1. The winds were light during this period and, therefore, the stratification is considered representative of the calm stage.

115   Reference fields only depend on depth. The current study focuses on the upper 55 m of the water column. Below this depth, an isothermal layer around 20 m thick was found, which facilitated the implementation of appropriate boundary conditions (see below).

Solar radiation is the only energy source considered during the idealized calm period. The daily incoming shortwave radiation, I_o, was obtained from the Atmospheric Surface Flux Group (ASFG) tower logs at the ice station SHEBA (Persson et al., 2002),

120   Figure 2. The shortwave radiation records per hour were averaged from July 18th to July 26th 1998, to estimate the daily variation of the solar variable. For computational efficiency (see below), the averaged data was fitted to a target function

$F(t) = A \cos\left(\frac{2\pi t}{B} + \frac{2\pi}{C}\right) + D$, where the constants A, B, C and D were determined by the method of least-squares.

The albedo for the bare ice and open sea are 0.63 and 0.06, respectively (Bitz and Lipscomb, 1999; Pegau and Paulson, 2001). The solar radiation is absorbed by the water body and ice cap according to Beer's law with extinction coefficients λ of 0.08

125   m^{-1} and 1.5 m^{-1}, respectively (Jackson et al., 2010; Bettge et al., 1996). An average ice thickness of 2.6 m was obtained from measurements made in the area from July 18th to July 26th (Perovich, et al. 2007). Sea ice sheets melt due to incident solar radiation. The effects of melting on the geometry of ice sheets are not considered here and therefore, the study is applied to sea ice sheets large enough and in times short enough to maintain constant ice properties (e.g., geometry, mass, salinity).

A nonhydrostatic, Boussinesq, rotating, two-dimensional model is used in this study. The dynamical equations are given by:

130

$$\frac{\partial u}{\partial t} + u\frac{\partial u}{\partial x} + w\frac{\partial u}{\partial z} = -\frac{1}{\rho_0}\frac{\partial \delta p}{\partial x} + fv + \nu_T \nabla^2 u \qquad (1)$$

$$\frac{\partial v}{\partial t} + u\frac{\partial v}{\partial x} + w\frac{\partial v}{\partial z} = -fu + \nu_T \nabla^2 v \qquad (2)$$

$$\frac{\partial w}{\partial t} + u\frac{\partial w}{\partial x} + w\frac{\partial w}{\partial z} = -\frac{1}{\rho_0}\frac{\partial \delta p}{\partial z} - \frac{1}{\rho_0}\delta\rho g + \nu_T \nabla^2 w \qquad (3)$$

$$\frac{\partial u}{\partial x} + \frac{\partial w}{\partial z} = 0 \qquad (4)$$

135

For velocity components u, v, w and pressure (δp) and density (δρ) anomalies. At near frozen temperatures the density variation is more dependent on salinity than temperature. Thus the simple equation of state ρ=0.808 S+1000, where S is the

The Cryosphere
Discussions

salinity in g kg^{-1} is considered (Smith and Morison, 1998). The Coriolis parameter is f=1.4 10^{-4} s^{-1} and g=9.8 m s^{-2}. $\nu_T = \nu + \nu_E$ where ν=10^{-6} m^2 s^{-1} is the molecular viscosity and ν_E is the eddy viscosity coefficient that accounts for the effects of the sub-

140   grid scales. The parametrization of ν_E suggested by Smagorinsky (1963, 1993) is adopted here. This is one of the most popular subgrid scale models parameterizing eddy viscosity. Briefly, the Smagorinsky model assumes that ν_E is proportional to the absolute strain rate:

$$\nu_E = l_o^2 |S| \tag{5}$$

145   $$|S| = \sqrt{2 S_{ij} S_{ij}} \tag{6}$$

$$S_{ij} = \frac{1}{2}\left(\frac{\partial u_i}{\partial x_j} + \frac{\partial u_j}{\partial x_i}\right) \tag{7}$$

where $|S|$ is the absolute value of the strain rate tensor S_{ij} and $u_i = \{u, v, w\}$ is *i-th* velocity component along the $x_i = \{x, y, z\}$ direction. The mixing length scale l_o is parametrized using the Smagorinsky constant Cs, l_o=Cs Ls. C$_S$ has been tuned from 0.1

150   to 0.7 and it is set to 0.2 in the present study, which is a common default value. L$_S$ is a length scale representing a filtering width. Its value depends on the grid discretization. In two-dimensional flows, L$_S$ may be taken as the square root of the area of the computational element. Considering the symmetry of the present setting, the total viscosity ν_T is then given by:

$$\nu_T = \nu + \underbrace{(C_S L_S)^2 \sqrt{\left(\frac{\partial u}{\partial x}\right)^2 + \left(\frac{\partial w}{\partial z}\right)^2 + 0.5\left(\frac{\partial u}{\partial z} + \frac{\partial w}{\partial x}\right)^2 + 0.5\left(\frac{\partial v}{\partial x}\right)^2 + 0.5\left(\frac{\partial v}{\partial z}\right)^2}}_{\nu_E} \tag{8}$$

155

Free-stress boundary conditions $\frac{\partial u}{\partial z} = 0, \frac{\partial v}{\partial z} = 0, w = 0$ are prescribed at the open water surface and the bottom depth. Non-slip conditions (u=0, v=0, w=0) are specified at the sea ice plates. Finally, periodic boundary conditions are imposed at the lateral boundaries.

The temperature and salinity fields evolve according to the equations:

160

$$\frac{\partial \delta T}{\partial t} + u \frac{\partial \delta T}{\partial x} + w \frac{\partial \delta T}{\partial z} = K_T \nabla^2 \delta T + S_r - w \frac{\partial T_{ref}}{\partial z} + K_T \frac{\partial^2 T_{ref}}{\partial z^2} \tag{9}$$

$$\frac{\partial \delta S}{\partial t} + u \frac{\partial \delta S}{\partial x} + w \frac{\partial \delta S}{\partial z} = K_S \nabla^2 \delta S - w \frac{\partial S_{ref}}{\partial z} + K_S \frac{\partial^2 S_{ref}}{\partial z^2} \tag{10}$$

Where δT(x, z, t) and δS(x, z, t) are the temperature and salinity anomaly fields with respect to the reference fields T$_{ref}$(z) and

165   S$_{ref}$(z). A simple thermodynamic model is employed to compute the surface salinity flux at the top interface, the Q$_s$. Specifically, Q$_s$ is obtained from:

$$F = \frac{Q_m}{\rho_i L_f} \tag{11}$$

$$Q_s = F(S_o - S_i) \tag{12}$$

170

where F is the bottom melting rate, ρ_i is a characteristic sea ice density (900 kg m^{-3}), L$_f$ is the latent heat of fusion of sea ice (333 kJ kg^{-1}) and S$_i$ (4 psu) is the sea ice salinity content. Q$_m$ is the heat flux used to melt the bottom of the ice. Its value is calculated from the observed bottom melt rates of 0.4 cm d^{-1} in the calm period and 1.2 cm d^{-1} during the storm (Richter-Menge et al. 2001). The melting model (11) and (12) ignores many aspects of the sea ice thermodynamics, but it is complex

175   enough to capture the essential features of sea ice melt, required in the present idealized framework. Sr is the internal heat source that quantifies the volumetric absorption of the solar radiation by the water body (Mao et al, 2010):

$$S_r = H_o\, \lambda\, e^{\lambda z} \tag{13}$$

180 where λ and H_o have been previously defined. $K_{T,S}$ are defined by (Schumann, 1996):

$$K_{T,S} = k_{T,S} + \frac{\nu_E}{Pr_{sgs}} \tag{14}$$

where $k_T=10^{-7}$ m^2 s^{-1} ($k_S=10^{-9}$ m^2 s^{-1}) is the molecular thermal (salinity) diffusion and $Pr_{sgs}=0.4$ is the turbulent Prandtl number

185 of the subgrid scale motions (Schumann, 1996).

A Dirichlet boundary condition is prescribed at the bottom of the ice plates ($\delta T(t)=-0.05$ºC) and of the domain ($\delta T(t)=0.0$ºC). As it was mentioned before, the latter is justified by the existence of an isothermal layer below the selected domain. A Neumman boundary condition, $\frac{\partial \delta S}{\partial n} = 0$ where n is the direction normal to the boundary, is selected for the salinity field at the open sea surface and the bottom boundary. This boundary condition approximates a zero and negligible salt flux across the

190 open ocean interface and the domain bottom, respectively. Negative salt fluxes define the boundary conditions in the ice plates, representing the flow of fresh water due to ice melt. Salinity fluxes across this boundary vary in time, depending on the solar heating. Similarly to the velocity field, periodic boundary conditions in δT and δS are prescribed at the lateral boundaries. Initial conditions are $\delta T(x, z, 0) = 0$ and $\delta S(x, z, 0) = 0$ in the model domain.

The wind simulations initiated just after the calm period. The intensity of the wind linearly increased during one day up to a

195 nominal value of 6 ms^{-1}. This is an idealized numerical representation of the process observed by Richter-Menge et al. (2001) from July 27th to July 31st. A Galilean transformation of the system equations and boundary conditions was performed to simulate ice motion under windy conditions (Skyllingstad and Denbo, 2001). This approach keeps the domain geometry unchanged, avoiding remeshing the domain and speeding up numerical simulations. The wind stress τ exerted on the lead open surface was computing according to the equation:

200

$$\tau = \rho_a\, Cd\, U_{10}^2 \tag{15}$$

Here, ρ_a (1.2 kg m^{-3} is the density of air, Cd is a dimensionless constant with value 1.3 10^{-3} to leading order (Wróbel-Niedźwiecka et al., 2019) and U_{10} is the wind speed at 10 m high. The balance condition between the shear and wind stresses:

205

$$\tau = \rho_o \nu_T \frac{\partial u}{\partial z} \tag{16}$$

is assumed as surface boundary condition at the open lead.

2.2 Computational approach

210 A standard Galerkin finite element method has been employed to spatially discretize Eqs. (1-4) and (5-6). The domain geometry was tessellated into 17430 triangular elements with 8952 nodes for this purpose. The characteristic sizes of the elements range from 0.45 m at the open sea surface to 1.8 m at the lateral boundaries, Figure 3. The discretization results in an algebraic system of equations for the values of the fields at the corners of the triangular elements (nodes). Once solved, low-order piecewise polynomials are usually employed to interpolate the solution from the nodes to other locations in the physical
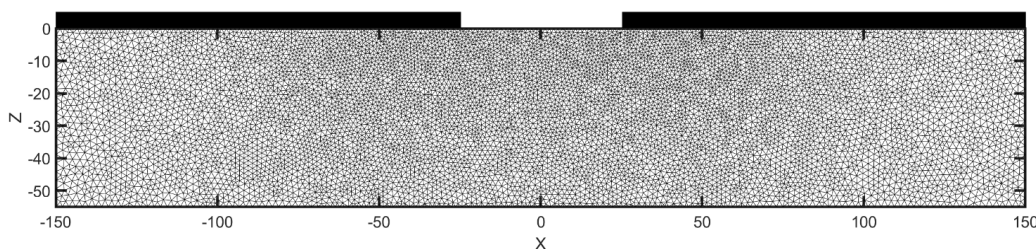
215

Figure 3: Triangular meshing of the computational domain. Black rectangles represent location of the sea ice cover.

220

domain. The specific mathematical expressions of the procedure are not replicated here, as they can be found in textbooks about finite elements (e.g., Dhatt and Touzot, 1984; Zienkiewicz and Taylor, 1995).

A fractional step method is selected to integrate in time Eqs. (1-4). The approach is based on an operator splitting that yields

225 a decoupling of the convection and diffusion of the velocity and the pressure, which acts to enforce the incompressibility constraint (Chorin, 1968). The time integration of the equations is performed by means of a Crank-Nicolson (implicit) time splitting for the convection and diffusion terms. An adaptive time step is chosen to ensure the stability of the numerical method. The full model run for five simulation days under calm conditions followed by another five days with wind.

230 **3 Results**

3.1 Calm period

The circulation during the fifth day is considered for the analysis of the calm period. Figure 4a shows the salinity distribution and current field obtained when the incoming solar radiation (336 Wm^{-2}) is maximum. Ice melting creates a layer of relatively

235 fresh water near the surface. There is a horizontal salinity gradient in this layer, with the freshest water below the ice caps rather than in the lead center. The horizontal density gradient derived from the salinity variation induces a circulation pattern with almost mirror symmetry with respect to the lead center, Figure 4a. The latter is described by near-surface convection cells that develop below the lead surface and the ice sheet up to 4 m depth. The velocity field converges at the geometric center of the open sea surface and diverges at about 2.5 m depth. The maximum velocity in the cells is 0.007 m s^{-1} in this snapshot. The

240 convection cells extend laterally for more than 40 m from the lead center. A northward (southward) flow of 0.005 m s^{-1} develops at the eastern (western) part of the domain.

Convection cells have profound implications for the spatial distribution of the thermal field during this period (Figure 4b). Specifically, surface currents inflowing from the lead sides accumulate warm waters in the lead center. At this location, warm waters are injected below the sea surface and distributed laterally by the convection cells (Figure 4b). The maximum

245 temperature is 1.1 ºC at the surface near the center of the lead. The temperature profile decays exponentially with depth to its reference value. The thermal drift is the result of heat transport from the surface and heating of subsurface layers in the lead due to solar radiation. A local temperature maximum results under the ice caps, Figure 4b. Local maximum temperatures are -0.9 ºC and -1 ºC at control stations located at 40 m east and west of the lead center, respectively. A net export of heat from the lead to the ice caps results from the convection cells. The heat outflows the lead region at depths ranging from 3 m to 5 m

250 and partially recirculates between 1 m to 2 m depth, due to the velocity pattern induced by the cells. The impact of the cell circulation is limited to the most superficial layers.
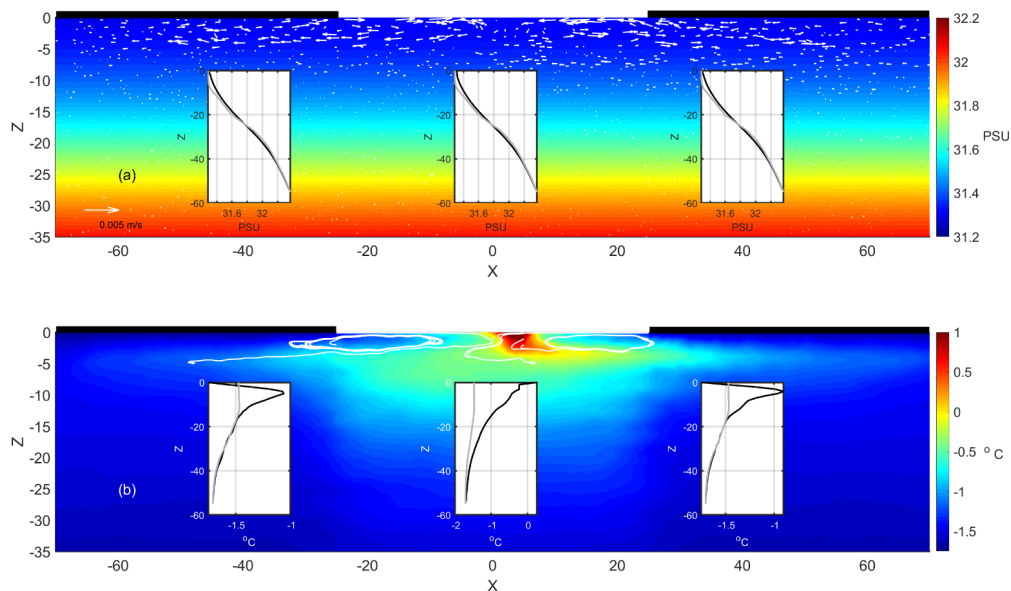
Figure 4: (a) Salinity and current fields and (b) temperature distribution and streamlines (white lines) at the end of the simulated
255 **calm period. The resolution of the current field is reduced to one tenth to facilitate visualization. The inserted plots in panels (a)**
and (b) compare the salinity and temperature profile (black lines) with their reference profiles at the lead center (x=0 m) and at the
locations x=-40 m and x=40 m, respectively.
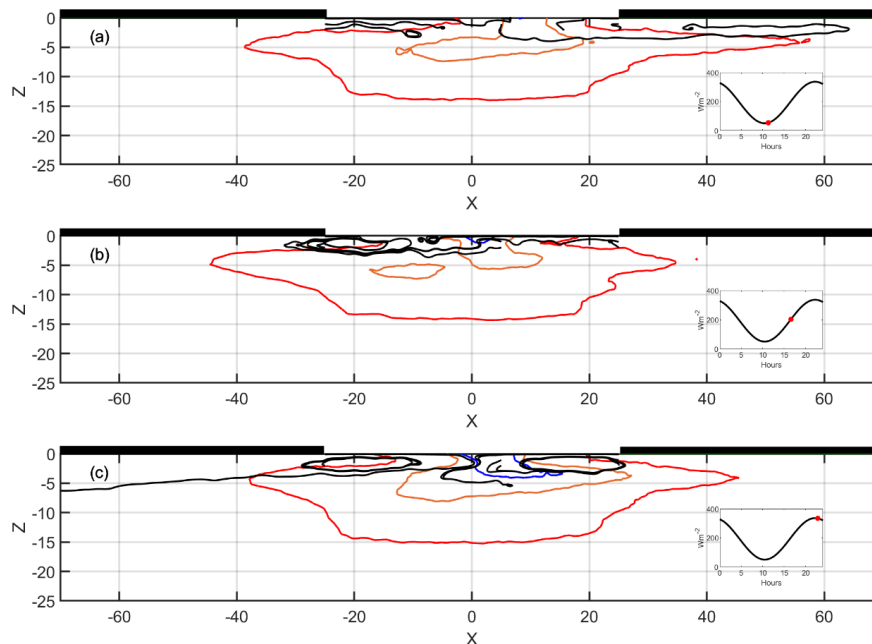
260 **Figure 5: Isotherms of temperature anomalies of -0.1 ºC (blue), -0.25 ºC (orange) and -0.5 ºC (red) and streamlines during different**
stages of incoming solar radiation. The inserted plots replicate Figure 2 to facilitate interpretation. The red dot indicates the solar
forcing of the corresponding subplot.

The circulation pattern of the cells is not static but undergoes variations due to the external forcing and internal dynamics,

265   Figure 5. The cells are not evident at the minimum of the solar heating (50 Wm^{-2}), existing only the residual thermal structure of previous heating events, Figure 5a. Cells appear when solar heating increases. Figure 5b shows the initial development of a cell on the western edge of the lead when solar radiation is 190 Wm^{-2}. The increase in solar radiation (336 Wm^{-2}) results into a state with two fully developed cells on both edges of the channel. In addition to this daily cycle, the cell circulation pattern is also modulated by the inertial frequency. Inertial modulations are tracked using the bulk horizontal location of certain

270   isotherms. In particular, the isotherm corresponding to -0.5 ℃ turned out to be a good indicator of where warm surface waters sink due to the circulation pattern. The bulk horizontal displacement varies mainly with the inertial period, Figure 6. Therefore, the cells alternately stretch and contract due to the inertial oscillations.

3.2 Wind period

275   An easterly wind is triggered in the model after the calm period. The intensity of the wind force ramped up during one day until a constant wind speed of 6 ms^{-1} for the remaining days. Ice sheets are assumed to move westward with the wind at a speed equal to two per cent of the wind speed, which is a common wind factor for ice sheets (Leppäranta, 2011). At the end of the simulation period, a westward current results from the wind and the motion of the ice (Figure 7a). The maximum velocity of the westward current is 0.15 ms^{-1} at the lead surface and reduces to 0.01 ms^{-1} at 10 m depth. Salinity is homogenized in the

280   water column due to the mixing derived from the wind and the ice motion. The mixing effect is more evident at the near-surface temperature (Figure 7b). The snapshot shows a plume at the trailing edge of the moving ice plate. The thermal plume is caused by the subduction of warm water under the ice due to westward motion. The heat accumulated by the penetration of solar radiation on the lead surface, diffuses rapidly in the upper layers.

A local temperature maximum results at a depth of about 28 m depth as a consequence of the action of the surface stress,

285   Figure 7b. The maximum temperature deepens and reduces its value during the progress of the simulation (Figure 8). The numerical results suggest that the maximum temperature results from the erosion of the initial thermal profile generated during the calm period. The vigorous entrainment, mixing and diffusion of fresh water from melting sea ice driven by currents and turbulent transport, removes heat stored during the calm period in the near-surface layers. This generates temperatures in the upper layers that are lower than in the deeper layers, where the impact of surface stress is weaker and therefore the heat stored

290   during the calm period is partially conserved. The warm waters stretch horizontally under the action of the surface shear. Thus an NSTM layer is formed.

## 3.3 Sensitivity studies

3.3.1 Buoyancy forcing

295   A first sensitivity study explores the impact of meltwater runoff on the results described above. The numerical simulations were carried out considering half and double of the reported rate of meltwater runoff, keeping the other parameters the same as in the previous case. This subsection discusses the sensitivity of the NSTM layer to variation in meltwater runoff. From now on, only the resulting thermal field is considered.

Similarly to the case found in Subsection 3.2, the initial warm core stretches horizontally under the action of the surface shear

300   when the melt rate is halved (Figure 9a). However, the local maximum temperature of -1.5 ℃ is now at a depth of 17 m. Figure 9a shows the formation of Kelvin-Helmholtz waves at the interface between the most superficial layers and the NSTM layer. The instability is triggered by the relative motion and density difference between the layers. The bulk Richardson number is 1.2, close to the critical value when the Kelvin-Helmholtz instability is fully developed (Richardson number less than 0.25).

The NSTM layer deepens (28 m depth) and cools down (-1.6 ℃) by doubling the initial rate of meltwater runoff, Figure 9b.

305   The structure of the NSTM layer closely resembles the solution displayed in Figure 7b. The bulk Richardson number is about 0.3 for both cases, resulting in a near turbulent interface between the NSTM and overlying layers.
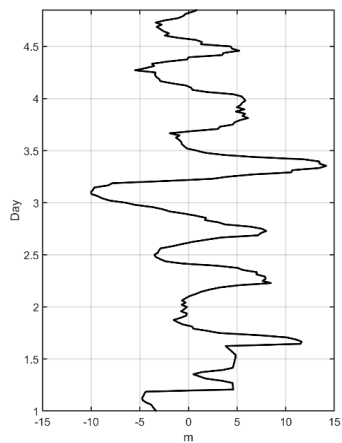
Figure 6: Time evolution of the bulk horizontal coordinate of the isotherm corresponding to -0.5 ºC.
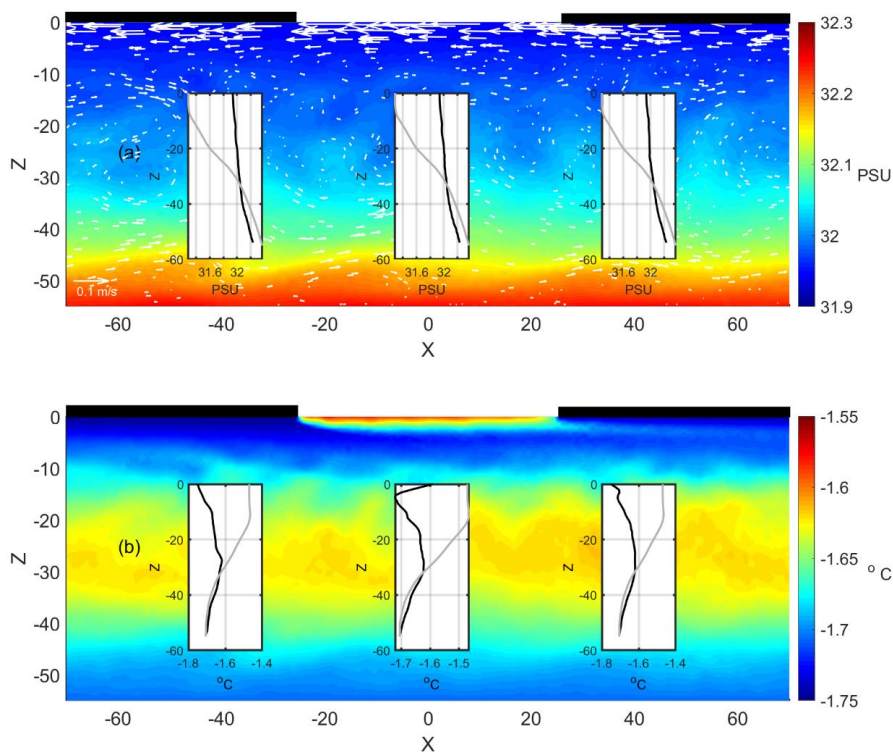
Figure 7: Similar to Figure 4 but at the end of the simulated wind period with a wind speed of 6 ms^{-1} and wind factor of 2 %. The Figure represents now the full water column to highlight the near-surface temperature maximum layer.

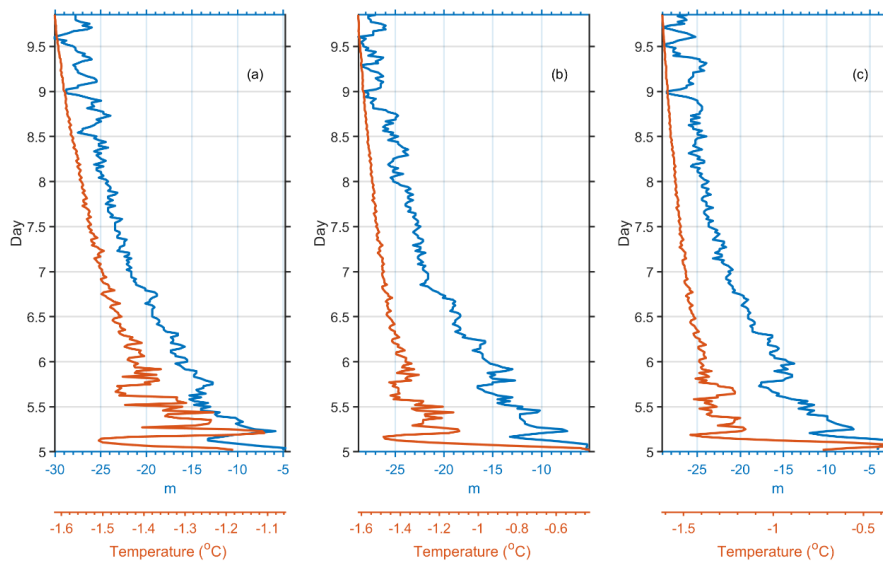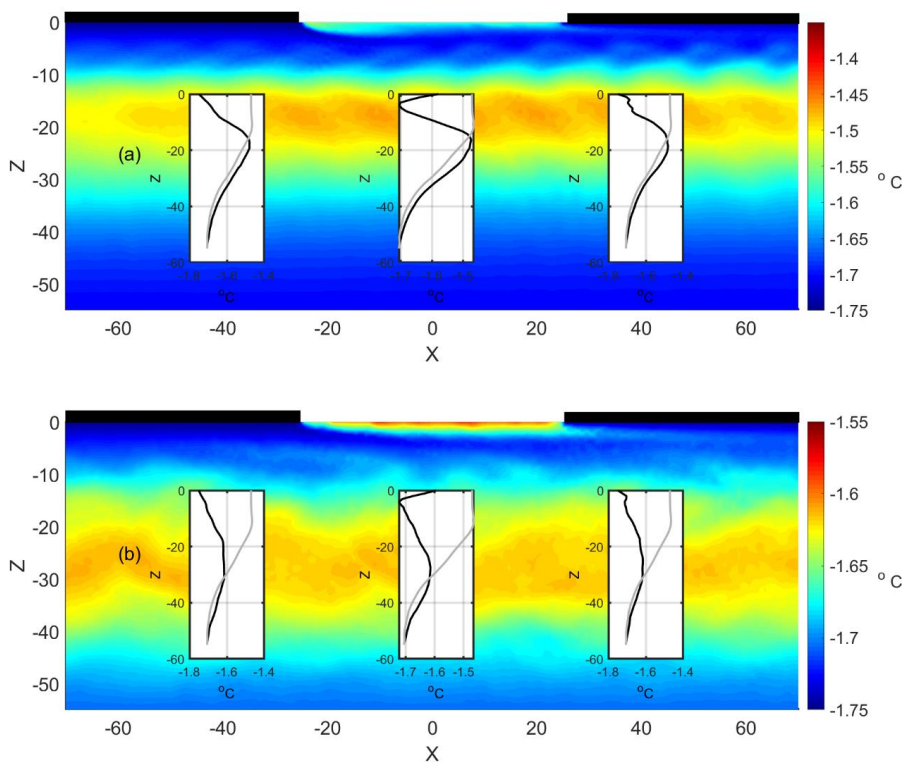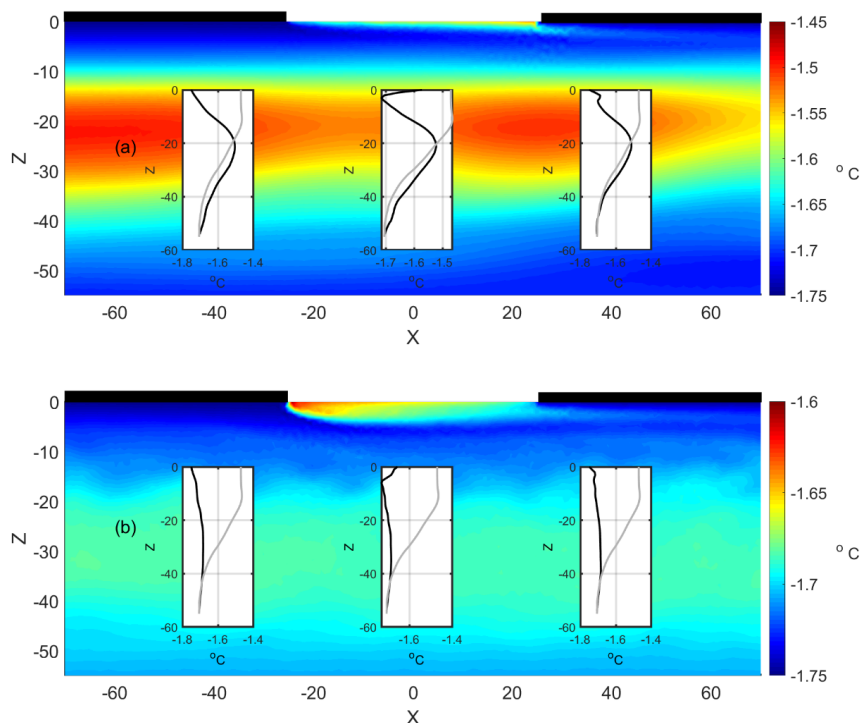**Figure 8: Evolution of the local maximum temperature (orange line) and its corresponding depth (blue line) in the control stations at (a) x= -40 m, (b) x=0 m and (c) x=40 m.**

320

Figure 9: Similar to Figure 7b but for the case with (a) half and (b) double of the reported melting rate.

11

Figure 10: Thermal distribution at the end of the simulated wind period with wind intensities of (a) 3 ms⁻¹ and (b) 9 ms⁻¹. The inserted plots in panels (a) and (b) compares the salinity and temperature profile (black lines) with their reference profiles at the lead center (x=0 m) and in the control stations at x=-40 m and x=40 m, respectively.

*3.3.2 Wind Forcing*

Additional simulations were carried out considering wind intensities of 3 ms⁻¹ and 9 ms⁻¹. The initialization, wind forcing ramp up and ice motion followed the procedure reported in Subsection 3.2. Under light wind conditions (3 ms⁻¹), the NSTM layer is shallower (20 m depth) and warmer (-1.51 °C), Figure 10a, than in the baseline simulation, Figure 7b. The original core of warm waters under the lead spreads horizontally as it moves west, leaving a trail of warm water at the tail. This generates a horizontal thermal anisotropy in the propagation depth of the warm core. Unlike in Figure 7b, no significant development of instabilities is observed along the warm layer.

A local temperature maximum is almost negligible at 30 m depth when the wind intensity is 9 ms⁻¹, Figure 10b. The thermal profile varies from temperatures close to freezing point in the surface layers to an almost homogenized thermal background below 20 m depth. The thermal maximum exceeds the background by only few hundredths of a degree. Unlike the cases discussed above, the core of slightly warmer waters is now horizontally homogenized. Thermal heating at the lead surface is uncoupled and does not have a significant impact on the NSTM layer during periods of wind and ice motion.

3.3.3 Ice motion

As part of the sensitivity studies, a set of numerical simulations evaluated the comparative relevance of the two sources of surface shear stress: wind and ice motion. Initially, a period of wind with a wind intensity of 6 ms⁻¹ and static sea ice conditions, was considered. A second simulation with the same wind intensity but with a wind factor of one per cent
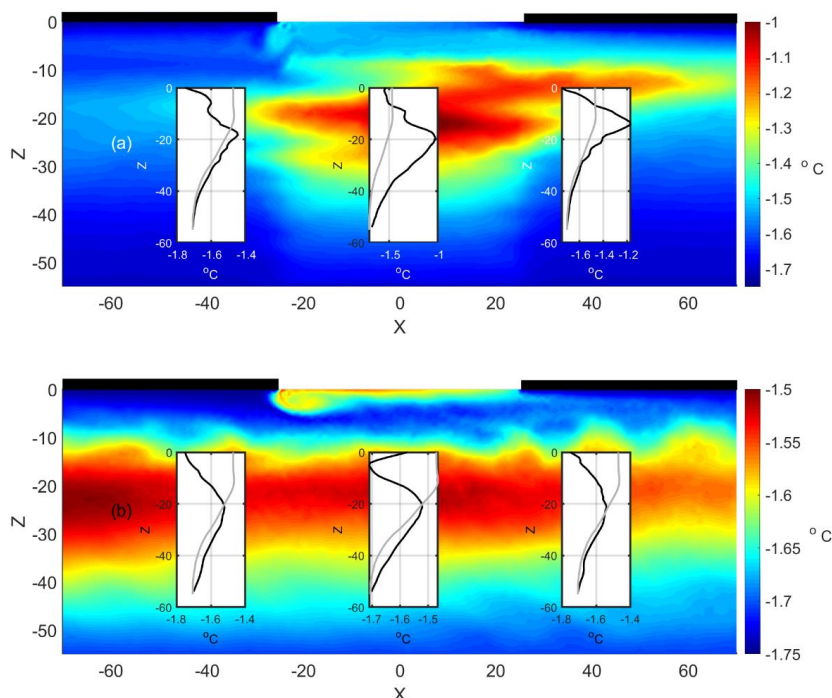
Figure 11: Thermal distribution at the end of the simulated wind period with wind intensity 6 ms⁻¹ and wind factors of (a) 0 % and (b) 1 %. The inserted plots in panels (a) and (b) compares the salinity and temperature profile (black lines) with their reference profiles at the lead center (x=0 m) and in the control stations located at x=-40 m and x=40 m, respectively.

of the wind speed, complemented the motionless ice case in addition to the results displayed in Figure 7b. Again, initialization and wind forcing ramp up followed the procedure detailed in Subsection 3.2. In the static sea ice configuration, the warm core generated under the lead during the calm period is distorted by the surface and near-surface currents induced by the wind stress and the boundary conditions at the fixed edges of the sea ice, Figure 11a. A westward surface current results in the lead surface by wind action. At the edge of the sea ice, the surface current deepens and bifurcates into a westward branch beneath the ice, and an eastward recirculation that crosses the lead and penetrates below the eastern sea ice sheet. The near-surface current generates shear in the shallower layers (10-15 m depth) of the warm water masses under the lead. Instead, the maximum temperature remains located below the center of the lead.

The results differ significantly with sea ice drift, Figure 11b. An NSTM layer is distributed horizontally at 20 m depth throughout the domain. The temperature distribution is not homogenous in its core, but scattered patches of the original NSTM core are still identified. For this value of the wind factor, the NSTM layer is warmer and shallower than the case shown in Figure 7b.

4 Discussion

Motivated by observations, this study has analysed the relationship between the oceanography below a summer lead exposed to a sequence of calm and moderate wind conditions and the formation of the NSTM layer. Conceptually, the hypothesis assumes that, during the calm period, summertime leads are preferential locations to accumulate heat from solar radiation. A subsequent wind event would deepen and horizontally distribute the excess heat accumulated during the calm period under the

lead. The horizontal dispersion of heat would be along the direction of wind and ice drift. The theoretical framework used to

370 test the hypothesis considers an idealized scenario that captures the fundamental physical aspects of the problem. These are defined by incoming solar radiation, sea ice melting, lead geometry, winds and ice drift. Other forcing such us longwave radiation, latent and sensible radiation heat fluxes and surface waves that would exist under real environmental conditions, were not analysed in this study. Paulson and Pegau (2001) reported net average values of -25, 5 and 3 W m^{-2} for the longwave radiation, sensible and latent heat fluxes, respectively, in a lead during summer. The sum of the net radiative, sensible and

375 latent heat fluxes is small compared with the incoming shortwave radiation and therefore has minimal impact on dynamics at the time scale considered. Finally, wind fetch is quite limited within the leads preventing the full development of the wave field (Pegau and Paulson, 2001). This is especially true in small leads.

Although the study is carried out in an idealized framework, its design, initial conditions and forcing closely follow the observations made from July 18th to July 31st 1998 at SHEBA station. In particular, the conditions during the calm period are

380 derived from the observations obtained from July 18th to July 26th, while the period from July 27th to July 31st determined certain aspects of the simulations with wind. Unfortunately, the dynamical disparity and the geometric dissimilarity between the idealized framework and the real evolution prevent comparison between model results and observations. In particular, Richter-Menge et al. (2001) reported drastic changes in ice field geometry after the storm that are not captured here.

The representation of the sea ice sheet in this work follows the same geometrical description found in previous numerical

385 studies considering leads of similar scales (Kozo, 1983; Smith and Morison, 1993; Smith and Morison, 1998). These are represented by appropriate kinematic and thermodynamic boundary conditions at the sea surface, with no subsurface sea ice structure. Therefore, the proposed idealization excludes the effects of melting at the lateral edge of the sea ice sheet and the effects of the kinematic boundary due to the roughness of the sea ice bottom. The former is negligible for total meltwater runoff due to the small ratio of leading edge area to bottom/surface area of the ice cover (Skyllingstad et al., 2005). For the

390 latter, roughness of the sea ice bottom would tend to increase turbulent mixing below the ice sheet, reducing the difference in density between bottom mixed meltwater runoff and the underlying ocean. Its effect is negligible during the calm period, due to the low speeds of the current (less than 0.01 m s^{-1}) resulting from the lateral buoyancy gradients between the edges and center of the lead. Instead, the roughness of the sea ice bottom could be a major factor in the formation of the boundary layer at the bottom of moving ice sheets. A detailed quantification of its impact would require a study at finer scales than those

395 considered in this work.

The proposed scenario has been formalized mathematically in terms of a nonhydrostatic, Boussinesq, rotating, two-dimensional model. This mathematical description is common for simulating leads (Kozo, 1983; Smith and Morison, 1998) because it takes full advantage of the symmetry of the lead geometry to reduce the dimensionality of the problem. Its validity is restricted to the lead region away from the boundaries and openings. A detailed simulation of the thermodynamics and

400 dynamics of sea ice is out of the scope of the present study. Instead, a methodology is required to provide reasonable boundary conditions for salinity fluxes from the melting ice sheet. In this work, the salinity fluxes resulting from the melting of sea ice have been parametrized based on the observations reported by Richter-Menge et al. 2001. A daily variability of the melt rate assumes a dependence with the incoming solar radiation while its daily average is equal to the value observed during the calm period. In the absence of observational support, it is assumed that excess melt during the wind period results from basal melting

405 by ocean heat flux. The value of this melting component is constant during the simulated daily cycle.

A daily generation of convection cells near the surface, results under the lead and the ice sheet during the calm period. These result from the combination of lead geometry, solar heating and the melting of sea ice. The convection cells are permanently active during the summer, but with their intensity modulated by the incoming solar radiation cycle. They disappear when solar heating is below a threshold value of about 80 W m^{-2}. Although relatively restricted to the near-surface layer, convection cells

410 have been revealed as an important mechanism for determining the thermodynamics of the mixed layer under the lead. Convection cells routinely pump heated surface waters below the surface at the lead center. This causes, together with the

subsurface heating and heat diffusion, water masses below the lead warmer than the surrounding environment. Masses of warm water also extend horizontally below the ice sheet as a result of the circulation pattern. The patch of masses of warm waters stretches and deepens during the period of maximum solar radiation and contracts when solar heating is minimum. A net

415 stretching and deepening results from the daily cycle process. This mechanism could explain the deepening and lateral spreading under the adjacent ice of warm water masses, observed by Richter-Menge et al., (2001) in summertime leads under persistent calm conditions. Warm water masses are also subject to asymmetric horizontal displacements/distortions induced by inertial motions.

A windy period after the calm conditions modifies the previously reported thermal conditions. Shear stress occurs in the
420 uppermost layers from the wind and/or ice drift. Regardless of the conditions of ice movement, warm water masses become uncoupled from the sea surface. A cold layer of melt runoff insulates the warm water masses from the sea surface, generating a NSTM layer in the numerical results. The NSTM layer develops over ranges of depth and temperature (depending on wind and ice speeds) consistent with observations. In the absence of ice drift, the NSTM layer remains localized below the lead. It is dispersed laterally with the motion of the ice due to the surface shear stress. The NSTM layer survives under moderate wind
425 and associated ice motion, disappearing for wind intensities greater than 9 ms^{-1}.

Numerical simulations suggest that the sequence of calm and windy periods in the leads results in a final thermal structure characterized by a spatially distributed NSTM layer, whose depth and temperature depend on the intensity of the wind and the conditions of ice motion. The calm period represents a conditioning phase of the NSTM layer, where heat from incoming solar radiation accumulates below the lead and adjacent areas. The subsequent wind-injected shear stress and ice drift induces
430 turbulent mixing between the warm waters and melt runoff in the upper layers. Mixing reduces the temperature of the superficial layers below the values of the lower layers, the latter being less exposed to the action of the surface forcing. Higher forcing and mixing results in a deeper and cooler NSTM layer, as observed in the simulations. The NSTM layer remains detached and isolated from the sea surface by a layer of cooler, fresher water. This numerical result supports the hypotheses that attribute the resilience of the NSTM layer to the protective action of the upper layer on the underneath ones (Maykut and
435 McPhee, 1995; Jackson et al., 2010; Gallaher et al., 2017). Unlike previous protection assumptions, a halocline separating the upper layer from the protected layers does not appear in the numerical simulations. This could be the consequence of the inevitable diffusive character of numerical models. Alternatively, the reported halocline may develop after the mixing period and being absent during the wind event.

A significant increase in warming of the upper Arctic Ocean has been observed in the last decades (Steele et al., 2008). During
440 the summer, part of the heat from incoming solar radiation is stored in the NSTM layer formed between mid-June and mid-July (Jackson et al., 2010). Although the formation of the NSTM layer is still under debate, there is a scientific consensus in attributing the development of the NSTM layer to the absorption of solar radiation penetrating the upper ocean through the leads and melt ponds (Maykut and McPhee, 1995; Jackson et al., 2010). However, this mechanism does not exclude other processes. Steele et al. (2011) found, using a Pan-Arctic circulation model, an additional NSTM formation process originating
445 from open water surface cooling. In addition, Gallaher et al. (2017) highlight from observations and a 1-D boundary layer model the relevance of seasonal buoyancy and wind events to facilitate the development of the NSTM layer. The present study supports this last finding and complements it by including the action of ice motion. In general, the evidence seems to confirm that processes or mechanisms at different scales can participate in the formation of the NSTM layer.

If predictions are accurate, climate change is expected to lead to a nearly ice-free Arctic Ocean in summer within a few decades.
450 This hypothetical scenario involves the replacement of the robust multi-year sea ice by a weaker young ice. This would facilitate the formation of melted leads at the beginning of the melting season, increasing their frequency in the ice sheet. Therefore, the effects of lead-scale oceanographic processes (including the one reported in this study) may increase their global relevance. A particular motivation for this author is that the expected future warming and deepening of the NSTM layer may result in a sound channel similar, but with a different physical origin, to the "Beaufort lens" discovered in the Canadian Arctic

The Cryosphere
Discussions
Open Access
EGU

455 (Freitag et al., 2015). Assessing the mechanisms of formation of the NSTM layer, its physical properties, resiliency along the year and its geographical distribution is of special relevance to determine the underwater soundscape in the future Arctic Ocean, with an impact on the vertical variability of ambient noise and the communication performance of marine mammals.

Competing interests

The author declares that he has no conflict of interest.

References

Alam, A. and Curry, J., Lead-induced atmospheric circulations. J. Geophys. Res. Oceans, 100, 4643–4651, doi:10.1029/94JC02562, 1995.

Barry, R. G., Miles M. W., Cianflone R. C., Scharfen, G. and Schnell, R. C., Characteristics of Arctic sea ice from remote
470 sensing data and their relationship to atmospheric processes. Ann. Glaciology, 12, 9-15, doi:10.3189/S0260305500006893, 1989.

Bettge, T. W., Weatherly, J. W. Washington, W. M. Pollard, D., Briegleb, B.R. and Strand, W. G. Jr., The NCAR CSM sea ice model. Boulder, CO, National Center for Atmospheric Research. (NCAR Tech. Note NCAR/TN-425+STR), 1996.

Bitz, C. M. and Lipscomb, W. H., An energy-conserving thermodynamic model of sea ice. J. Geophys. Res., 104, 15669-
475 15677, doi:10.1029/1999JC900100, 1999.

Brohan D. and Kaleschke, L., A nine year climatology of Arctic sea ice lead orientation and frequency from AMSR-E. Remote Sens., 6, 1451-1475, doi:10.3390/rs6021451, 2014.

Chorin, J. A., Numerical solution of the Navier-Stokes Equations. Math. Comp. 22, 745-762, doi:10.1090/S0025-5718-1968-0242392-2, 1968.

480 Dhatt, G. and Touzot, G., The finite element displayed, John Wiley & Sons Inc, New York, pp. 510, doi: 10.1002/9781118569764, 1984.

Douglas, T., Sturm, M., Simpson, W., Brooks, S., Lindberg, S. and Perovich, D., Elevated mercury measured in snow and frost flowers near arctic sea ice leads. Geophys. Res. Lett., 32, L04502, doi:10.1029/2004GL022132, 2005.

Freitag, L., Koski, P., Morozov, A., Singh, S. and Partan, J., Acoustic communications and navigation under Arctic ice, 2012
485 Oceans, Hampton Roads, VA, 1-8, doi:10.1109/OCEANS.2012.6405005, 2012.

Freitag, L., Ball, K., Partan, J., Koski, P., and Singh, S., Long range acoustic communications and navigation in the Arctic, OCEANS 2015 - MTS/IEEE Washington, Washington, DC, 1-5, doi:10.23919/OCEANS.2015.7401956, 2015.

Gallaher, S. G., Stanton, T. P., Shaw, W. J., Kang, S. H., Kim, J. H. and Cho, K. H., Field observations and results from a 1-D boundary layer model for developing near-surface temperature maxima in the Western Arctic, Elem. Sci. Anth., 5, 1-21,
490 doi:10.1525/elementa.195, 2017.

Grenfell, T. C. and Maykut, G. A., The optical properties of ice and snow in the Arctic Basin. J. Glaciol, 18, 445-463, doi:10.3189/S0022143000021122, 1977.

Haggerty, J. A., Maslanik J. A., Curry, J. A., Heterogeneity of sea ice surface temperature at SHEBA from aircraft measurements, J. Geophys. Res., 108, 8052, doi:10.1029/2000JC000560.

495 Hoffman P. J., Ackerman S. A., Liu, Y. and Key J. R., The detection and characterization of Arctic Sea ice leads with satellite imagers, Remote Sens., 11, 521, doi: 10.3390/rs11050521, 2019.

Jackson, J. M., Carmack, E. C., McLaughlin, F. A., Allen, S. E., Ingram, R. G., Identification, characterization and change of the near-surface temperature maximum in the Canadian Basin, 1993-2008, J. Geophys. Res., 115, C05021, doi:10.1029/2009JC005265, 2010.

500 Kadko, D., Modeling the evolution of the Arctic mixed layer during the fall 1997 Surface Heat Budget of the Arctic Ocean (SHEBA) Project using measurements of 7Be. J. Geophys. Res., 105, 3369-3378, doi:10.1029/1999JC900311, 2000.

Kort, E. A., Wofsy, S. C., Daube, B. C., Diao, M., Elkins, J. W., Gao, R. S., Hintsa, E. J., Hurst, D. F., Jimenez, R., Moore, F. L., Spackman, J. R. and Zondlo, M. A., Atmospheric observations of Arctic ocean methane emissions up to 82 degrees north, Nat. Geosci., 5, 318–321, doi:10.1038/ngeo1452, 2012.

505 Kozo, T., Initial model results for Arctic mixed layer circulation under a refreezing lead. J. Geophys. Res., 88, 2926-2934, doi: 10.1029/JC088iC05p02926, 1983.

Lemke, P., Manley, T.O., The seasonal variation of the mixed layer and the pycnocline under polar sea ice, J. Geophys. Res., 89, 6494-6504, doi:10.1029/JC089iC04p06494, 1984.

Leppäranta, M., The drift of sea ice. Springer Science & Business Media, 350 pp., doi:10.1007/978-3-642-04683-4

510 Levermann, A., Mignot, J., Nawrath, S. and Rahmstorf, S., The role of northern sea ice cover for the weakening of the thermohaline circulation under global warming, J. Climate, 20, 4160–4171, doi:10.1175/JCLI4232.1, 2007.

Liu, J., Curry, J. A., Wang, H., Song, M. and Horton, R. M., Impact of declining Arctic sea ice on winter snowfall, P. Natl. Acad. Sci. USA, 109, 4074–4079, doi:10.1073/pnas.1114910109, 2012.

Mao, Y., Lei, C. and Patterson, J. C., Characteristics of instability of radiation-induced natural convection in shallow littoral

515 waters. Int. J. Thermal Sci., 49, 170-181, doi:10.1016/j.ijthermalsci.2009.07.004, 2010.

Maykut, G.A. Energy exchange over young sea ice in the central arctic. J. Geophys. Res. Oceans, 83, 3646–3658, doi:10.1029/JC083iC07p03646, 1978.

Maykut G.A. and McPhee, M. G., Solar heating of the Arctic mixed layer. J. Geophys. Res. Oceans, 100, 24691–24703, doi: 10.1029/95JC02554, 1995.

520 Miles, M.W. and Barry, R.G., A 5-year satellite climatology of winter sea ice leads in the western arctic. J. Geophys. Res. Oceans, 103, 21723–21734, doi:10.1029/98JC01997, 1998.

Morison, J., Smith, J. D., Seasonal variations in the upper Arctic Ocean at observed at T-3. J. Geophys. Res., 8, 753-756, doi: 10.1029/GL008i007p00753, 1981.

Morison, J. H., McPhee, M. G., Curtin, T. B. and Paulson, C. A., The oceanography of winter leads, J. Geophys. Res. Oceans,

525 97, C7, 11199-11218, doi:10.1029/92JC00684, 1992.

Morison J. H., McPhee, M. G., Lead convection measured with an autonomous underwater vehicle, J. Geophys. Res., 103, 3257-3281, doi:10.1029/97JC02264, 1998.

Paulson, C. A. and Pegau, W. S., 'The Summertime Thermohaline Evolution of an Arctic Lead: Heat Budget of the Surface Layer', in Sixth Conf. on Polar Meteorology and Oceanography, San Diego, CA, Am. Meteorol. Soc., Proceedings, 271-274,

530 2001.

Pegau, W. S. and Paulson, C. A., The albedo of Arctic leads in summer, Ann. Glaciol., 33, 221-224, doi: 10.3189/172756401781818833, 2001.

Perovich, D. K., Richter-Menge, J. A. and Tucker W. B. III, Seasonal changes in Arctic sea-ice morphology, Ann. Glaciol., 33, 171-176, doi:10.3189/172756401781818716, 2001.

535   Perovich D., Grenfell T. C., Light B, Richter-Menge J., Tucker III W. B. and Ricken H., Ice Mass Balance. Version 1.0.
      UCAR/NCAR - Earth Observing Laboratory. doi:10.5065/D6H130DF, 2007.

      Persson, P. O. G., Fairall C. W., Andreas E. L., and Guest, Measurements of the meteorological conditions and surface energy
      budget near the atmospheric surface flux group tower at SHEBA. J. Geophys. Res., 107, C-10, SHE 21-1-SHE 21-35287–304,
      doi:10.1029/2000JC000705, 2002.

540   Ramudu E., Gelderloos R., Yang D., Meneveau, C., Gnanadesikan A., Large eddy simulation of heat entrainment under Arctic
      sea ice. J. Geophys. Res., 123, 287–304, doi:10.1002/2017JC013267, 2018.

      Richter-Menge, J. A., Perovich, D. K. and Pegau, W. S., Summer ice dynamics during SHEBA and its effect on the ocean heat
      content, Ann. Glaciol., 33, 201-206, doi:10.3189/172756401781818176, 2001.

      Schumann, U., Direct and large eddy simulations of stratified homogeneous shear flow, Dyn. Atmos. Oceans, 23, 81-98,
545   doi:10.1016/0377-0265(95)00423-8, 1996.

      Schweiger, A. J., Lindsay, R. W., Vavrus, S., and Francis, J. A., Relationship between Arctic Sea Ice and clouds during
      Autumn. J. Clim. 21, 4799–4810, doi:10.1175/2008JCLI2156.1, 2008.

      Screen, J. A. and Simmonds, I., The central role of diminishing sea ice in recent Arctic temperature amplification. Nature 464,
      1334–1337, doi:10.1038/nature09051, 2010.

550   Skyllingstad E. D., Denbo W. D., Turbulence beneath sea ice and leads: a couples sea ice/large eddy simulation study. J.
      Geophys Res., 106, 2477-2497, 2001.

      Skyllingstad E. D., Paulson C. A., Pegau W. S., Simulation of turbulent exchange processes in summertime leads, J. Geophys.
      Res., 110, C05021, doi:10.1029/2004JC002502, 2005.

      Smagorinsky, J., General circulation experiments with the primitive equations: I. the basic experiment. Mon. Wea. Rev., 91,
555   99-164, doi:10.1175/1520-0493(1963)091<0099:GCEWTP>2.3.CO;2, 1963.

      Smagorinsky, J., Some historical remarks on the use of nonlinear viscosities. Large Eddy Simulation of Complex Engineering
      and Geophysical Flows, B. Galperin and S. A. Orszag, Eds., Cambridge University Press, 3–36, doi:10.1002/qj.49712052017,
      1993.

      Smith, D.C. IV, Morison, J. H., A numerical study of haline convection beneath leads in sea ice, J. Geophys. Res., 98, 10,069-
560   10,087, doi:10.1029/93JC00137, 1993.

      Smith, D. C. IV, Morison J. H., Nonhydrostatic haline convection under leads in sea ice. J. Geophys. Res., 103, 3233-3247,
      doi:10.1029/97JC02262, 1998.

      Spielhagen, R. F. et al., Enhanced Modern Heat Transfer to the Arctic by Warm Atlantic Water, Science, 331, 450–453,
      doi:10.1126/science.1197397, 2011.

565   Stanton, T., and Shaw, B., SHEBA upper ocean CTD and thermal microstructure, Western Arctic Ocean. Boulder, Colorado
      USA: National Center for Atmospheric Research, ARCSS Data Archive, 2006.
      http://data.eol.ucar.edu/codiac/dss/id=106.ARCSS151

      Steele, M., Ermold, W. and Zhang, J., Arctic ocean surface warming trends over the past 100 years, Geophys. Res. Lett., 35,
      L02614, doi:10.1029/2009JC005849, 2008.

570   Steele, M., Ermold W., Zhang J., Modeling the formation and fate of the near-surface temperature maximum in the Canadian
      Basin of the Arctic Ocean, J. Geophys. Res., 116, C11015, doi:10.1029/2010JC006803, 2011.

      Steiner, N., Lee, W. and Christian, J., Enhanced gas fluxes in small sea ice leads and cracks: Effects on CO2 exchange and
      ocean acidification. J. Geophys. Res. Oceans, 118, 1195–1205, doi:10.1002/jgrc.20100, 2013.

      Stroeve, J., Holland, M. M., Meier, W., Scambos, T., and Serreze, M., Arctic sea ice decline: Faster than forecast, Geophys.
575   Res. Lett., 34, L09501, doi:10.1029/2007GL029703, 2007.

      Tschudi, M. A., J. A. Curry, and J. A. Maslanik, Characterization of springtime leads in the Beaufort/Chukchi Seas from
      airborne and satellite observations during FIRE/SHEBA, J. Geophys. Res., 107(C10), 8034, doi:10.1029/2000JC000541, 2002

Vihma, T., Effects of Arctic sea ice decline on weather and climate: a review, Surv. Geophys., 35, 1175–1214, doi:10.1007/s10712-014-9284-0, 2014.

580 Wernecke, A. and Kaleschke, L, Lead detection in arctic sea ice from Cryosat-2: Quality assessment, lead area fraction and width distribution. Cryosphere, 9, 1955–1968, doi:10.5194/tc-9-1955-2015, 2015.

Wilchinsky, A. V., Heorton H. D. B. S., Feltham D. L., and Holland, P. R., Study of the impact of ice formation in leads upon the sea ice pack mass balance using a new frazil and grease ice parameterization, J. Phys. Oceanogr., 45, 2025–2047, doi:10.1175/JPO-D-14-0184.1, 2015.

585 Wróbel-Niedźwiecka, I., Drozdowska, V., Piskozub, J., Effect of drag coefficient formula choice on wind stress climatology in the North Atlantic and the European Arctic, Oceanol., 61, 291-299, doi: 10.1016/j.oceano.2019.02.002, 2019.

Zhang, X., Sorteberg, A., Zhang, J., Gerdes, R. and Comiso, J. C. Recent radical shifts in atmospheric circulations and rapid changes in Arctic climate system. Geophys. Res. Lett. 35, L22701, doi:10.1029/2008GL035607, 2008.

Zienkiewicz, O. C. and Taylor, R. L., The finite element method. Basic formulation and linear problems, McGraw-Hill,

590 Maidenhead, pp. 648, doi:10.1002/nme.1620300312, 1995.